THE JOURNAL OF PHYSICAL CHEMISTRY LETTERS
A JOURNAL OF THE AMERICAN CHEMICAL SOCIETY

pubs.acs.org/JPCL Letter

Hot Carrier Dynamics at Ligated Silicon(111) Surfaces: A Computational Study

Yulun Han, Kweeni Iduoku, Gena Grant, Bakhtiyor Rasulev, Alexey Leontyev, Erik K. Hobbie, Sergei Tretiak, Svetlana V. Kilina, and Dmitri S. Kilin*

Cite This: *J. Phys. Chem. Lett.* 2021, 12, 7504−7511 Read Online

ABSTRACT: We provide a case-study for thermal grafting of benzenediazonium bromide onto a hydrogenated Si(111) surface using *ab initio* molecular dynamics (AIMD) calculations. A sequence of reaction steps is identified in the AIMD trajectory, including the loss of N_2 from the diazonium salt, proton transfer from the surface to the bromide ion that eliminates HBr, and deposition of the phenyl group onto the surface. We next assess the influence of the phenyl groups on photophysics of hydrogen-terminated Si(111) slabs. The nonadiabatic couplings necessary for a description of the excited-state dynamics are calculated by combining *ab initio* electronic structures and reduced density matrix formalism with Redfield theory. The phenyl-terminated slab shows reduced nonradiative relaxation and recombination rates of hot charge carriers in comparison with the hydrogen-terminated slab. Altogether, our results provide atomistic insights revealing that (i) the diazonium salt thermally decomposes at the surface allowing the formation of covalently bonded phenyl group, and (ii) the coverage of phenyl groups on the surface slows down charge carrier cooling driven by electron−phonon interactions, which increases photoluminescence efficiency at the near-infrared spectral region.

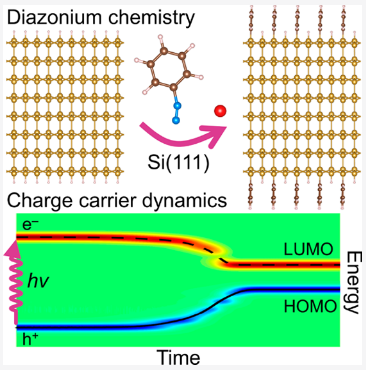

Silicon is one of the most technologically important materials with innumerous applications in microelectronics and photovoltaics. In order to take full advantage of silicon, it is essential to reduce the density of silicon dangling bonds at surfaces and interfaces. A widely used method in the semiconductor industry is chemical etching, in which silicon is treated with peroxide solutions followed by exposure to hydrogen fluoride solutions leading to hydrogen passivation of silicon surfaces.[1,2] However, Si−H bonds are not stable, and thus oxidation of silicon surface can take place within hours.[3] The presence of surface oxides further leads to electronic defects, which undermines the performance of silicon.[4,5]

The direct covalent grafting of alkyl groups onto silicon surfaces results in improved chemical and thermal stabilities,[4] while the packing density of alkyls on the silicon surface depends on the size of the ligand.[6] A variety of alkyl groups have been covalently linked to silicon surfaces.[7−16] With methyl groups, the complete coverage of silicon surface sites is achieved.[8] With ethyl groups the coverage is about 80%.[9] In most cases, the limiting coverage by long-chain or bulky alkyls is around 50%, with nonalkylated sites terminated by atomic hydrogen or hydroxyl groups.[13−15] The oxidation of silicon surfaces is inhibited greatly even under a partial alkyl coverage.[17] Using aryl diazonium salts to functionalize carbon, silicon, and metals is another well-known technique, allowing the formation of aromatic layers covalently bonded to the surface.[18−22] The reaction typically involves a homolytic dediazonation step and can be performed under a variety of conditions such as electrochemical reduction, ultrasonication, and heating.[20,23−27]

The optoelectronic applications of silicon rely on properties such as charge carrier mobility, the relative energy of valence band minimum (VBM) and the conduction band maximum (CBM), and the ability to absorb and emit photons, all of which may be affected by surface passivation. A better understanding of effects induced by surface passivation is thus critical for realizing the full potential of silicon for photovoltaics and light-emitting applications. First-principles calculations have been successfully used to describe ground state properties of many semiconductor materials. An accurate description of nonequilibrium dynamics related to hot carries and excited states requires treatment of coupling between electronic and nuclear degrees of freedom and goes beyond the Born−Oppenheimer approximation.[28,29] Prevalent methods (e.g., mean-field Ehrenfest,[30] surface hopping,[31,32] and Redfield[33,34]) are typically used to simulate such dynamics relying on nonadiabatic couplings. Such modeling incorporating nonadiabatic effects provides mechanistical pictures of photoexcited dynamics and nonradiative relaxation for molecular

Received: June 28, 2021
Accepted: July 27, 2021
Published: August 3, 2021

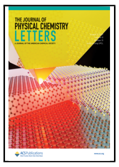

systems.[35−40] A broad variety of previous studies addressed excited state properties and dynamics of various silicon systems, such as photochemistry of silane molecules using surface hopping methods,[41] surface photovoltage of Si thin films by density matrix treatment,[42,43] multiple exciton generation in silicon−carbon nanotube quantum heterostructures through applying Boltzmann transport equation,[44] charge carrier relaxation for Si quantum dots,[45,46] nanowires,[47] and Si/Au nanointerfaces[48,49] adopting Redfield formalism, and nonradiative recombination in Si nanocrystals through the characterization of conical intersections.[50,51]

In this work, we report a case-study on thermal grafting of benzenediazonium bromide, a specific precursor from the class of diazonium salts, onto hydrogenated Si(111) surfaces using density functional theory (DFT) based *ab initio* molecular dynamics (AIMD) calculations. We explore this precursor to show its ability to bind to the Si surface and transform into a protective ligand. We also study the influence of phenyl groups on the optical and electronic properties of hydrogenated Si(111) slabs. We further describe charge carrier relaxation due to electron−phonon interactions using the reduced density matrix approach within the Redfield formalism.

Our simulations focus on two-dimensional model systems to minimize computational cost and explicitly account for surface effects. There are two atomic models considered in this work: hydrogenated and phenyl-covered Si(111) slabs. In the case of phenyl-covered slabs, half of the H atoms on the hydrogenated slab are replaced by phenyl groups, giving a chemical formula of $Si_{128}H_8Ph_8$. Note that the surface ligands are arranged in such a way that minimal steric hindrance is expected. The optimized geometries of various models used in this calculation are shown in Figure 1. Orbital energies, the spatial distribution of orbitals, and transition dipoles are obtained based on the geometry-optimized models. To study time-dependent electronic structures, AIMD calculations are performed using a time step of 1 fs with duration up to 1500 fs for each trajectory. There are two sets of AIMD calculations. The one at high temperature models chemical reactions from reactants to products by providing enough kinetic energies to overcome reaction barriers (see Figure S1). Representative examples using high-temperature AIMD to model chemical reactions are available in previous work.[52−54] The other one at ambient temperature serves as a foundation for computing nonadiabatic couplings and elements of the Redfield tensor, which describes excited-state dissipative dynamics of charge carriers. The methodologies for computing charge carrier dynamics can be found elsewhere.[55−57] All calculations are performed using periodic plane wave DFT within the Vienna Ab Initio Simulation Package (VASP).[58−62] The projected augmented wave (PAW)[63] potentials and the generalized gradient approximation (GGA)[64,65] with Perdew−Burke−Ernzerhof (PBE)[65] exchange-correlation functional are adopted for the calculations. The long-range internuclear interactions are treated with the semiempirical pairwise corrections (DFT+D2).[66] A plane wave energy cutoff is set as 500 eV. The Brillouin zone is only sampled at the gamma point, unless otherwise stated.

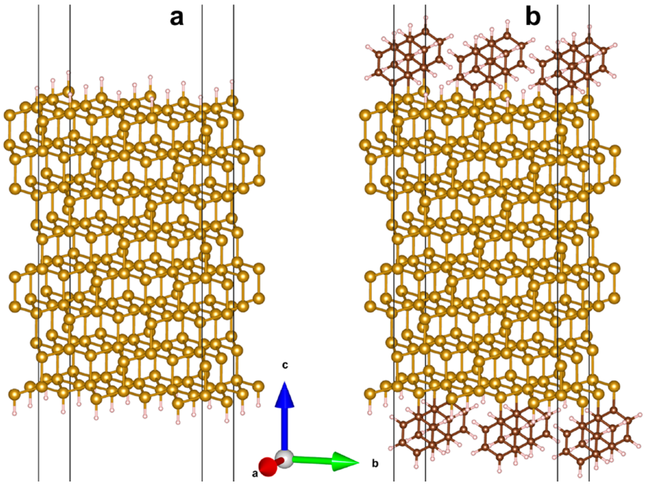

Figure 1. Optimized structures of (a) $Si_{128}H_{16}$ and (b) $Si_{128}H_8Ph_8$ slabs. The yellow, brown, and pink spheres represent Si, C, and H, respectively. The vacuum layer along the *z*-axis is not shown explicitly. Phenyl and H-termination are chosen to coexist to avoid steric repulsion.

First-principles calculations are first performed to model the thermal grafting of benzenediazonium bromide onto the hydrogenated silicon slab. Specifically, we carry out AIMD calculations at 2000 K to model the covalent surface chemistry. The use of high temperature ensures that chemical reactions occur at a short time scale, thus reducing the length of trajectories. To further reduce computational costs, only the diazonium salt and atoms at the top layer of the slab are allowed to move in our simulations. This is different from the setup of AIMD calculations at ambient temperatures, where all atoms freely move. To study the charge transfer events in the thermal grafting reaction, we further conduct Bader charge analysis[67−69] for snapshots along the trajectory, as detailed in Table S1. Figure 2 shows a representative AIMD trajectory at 2000 K. One first observes the elongation of C−N bond with time due to the electron transfer from the slab to the diazonium salt. Later on, the breaking of C−N bond occurs, leading to the loss of N_2. In the following trajectory, the N_2 molecule drifts away from the surface, whereas the bromine anion and phenyl radical gradually approach the surface. Meanwhile, H atoms of the slab are found to be labile, whereas Si atoms are displaced away from their equilibrium positions due to the high kinetic energy of the system. The elongation and contraction events of Si−Si bonds are abundant. At a later stage, a proton is transferred from the slab to the bromide ion forming HBr. The HBr molecule is rather stable for the rest of the trajectory as evidenced by the oscillation of H−Br bond with time. Si atoms on the surface become reactive after the proton transfer. Several events, including breaking and reforming of Si−Si bond leading to surface reconstruction, are thus observed. Finally, one finds that the phenyl radical is attached to the surface forming the Si−C bond.

Based on these simulations, a sequence of reaction steps is interpreted as follows. The thermal activation facilitates electron transfer from the surface to the diazonium salt, which generates a diazenyl radical.

$$\mathrm{PhN_2^{+}Br^{-} + H{-}Si(surf) \rightarrow (PhN_2^{\bullet})Br^{-} + H{-}Si^{+}(surf)} \tag{1}$$

The diazenyl radical gives rise to a phenyl radical through the breaking of a C−N bond and releases molecular nitrogen.

$$\mathrm{(PhN_2^{\bullet})Br^{-} \rightarrow (Ph^{\bullet})Br^{-} + N_2} \tag{2}$$

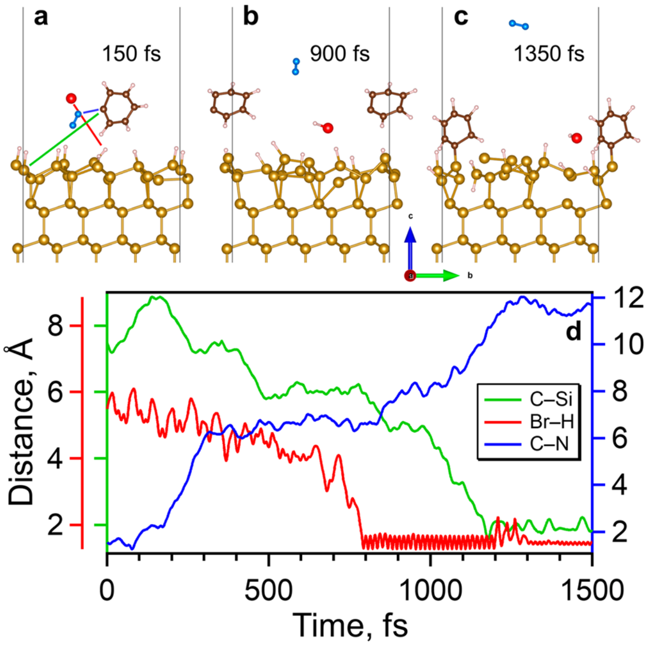

Figure 2. (a−c) Representative structural snapshots along the AIMD trajectory at 2000 K. (d) Time dependence of interatomic distances along the trajectory. Green, red, and blue solid lines correspond to C−Si, Br−H, and C−N distances, respectively. Simulations at high temperature mitigate computation cost and provide sufficient kinetic energy to overcome reaction barriers. This approach expedites the exploration of the phase space of nuclear configurations, evaluation of potential energy surfaces, and identification of reaction coordinates.[53] The slab is prevented from melting at such high temperatures by freezing the internal layers (i.e., fixing positions of these atoms).

The bromine anion approaches and polarizes the surface. A proton is then transferred from the surface, which forms and departs as HBr.

$$(\mathrm{Ph}^{\bullet})\mathrm{Br}^{-} + \mathrm{H{-}Si}^{+}(\mathrm{surf}) \rightarrow \mathrm{HBr} + \mathrm{Ph}^{\bullet} + {}^{\bullet}\mathrm{Si}(\mathrm{surf}) \qquad (3)$$

The proton transfer results in the unsaturated silicon surface site. Phenyl and surface Si radicals combine leading to the formation of a stable covalent Si−C bond.

$$\mathrm{Ph}^{\bullet} + {}^{\bullet}\mathrm{Si}(\mathrm{surf}) \rightarrow \mathrm{Ph{-}Si}(\mathrm{surf}) \qquad (4)$$

The identified sequence of reaction steps is consistent with reaction mechanisms proposed for the attachment of aryl groups onto hydrogenated Si substrates using diazonium salts, which have been validated by experimental data.[70,71]

We next focus on the influence of surface modification on the electronic structures of silicon slabs. Figure 3a shows the calculated density of states (DOS) for the $Si_{128}H_8Ph_8$ slab with an empirical broadening parameter of 0.01 eV for each state. The orbital energy is shifted with reference to the Fermi level, which is defined as the midpoint of the HOMO−LUMO gap. In the DOS, there are several features, in which a−e and a′−g′ correspond to states in the valence band (VB) and conduction band (CB), respectively. HOMO and LUMO states fall into the features a and a′, respectively. The HOMO−LUMO gap is 0.71 eV, which is underestimated due to the adoption of semilocal PBE functionals. On the other hand, the gap calculated with the more accurate hybrid HSE06 functional is about 1.37 eV. Compared to the bulk, the increase in gap is due to quantum confinement.[43] A more accurate description of the electronic and optical properties of silicon would require the use of a numerically expensive hybrid functional throughout the entire calculations or applying the “scissor operator” as a postprocessing step to adjust the gap.[43] Since this work focuses on a comparative study of various passivation aiming to identify trends, we believe that the numerically efficient PBE model is adequate for this purpose.

Figure 3b shows the calculated absorption spectrum of the $Si_{128}H_8Ph_8$ slab, where this result is based on the independent orbital approximation (IOA).[56] In a confined nanostructure of size r, the kinetic energy and the electron−hole Coulomb interaction scale as $1/r^2$ and $1/r$, respectively. For r approaching zero, the $1/r^2$ term provides the leading contribution. Therefore, for nanostructures smaller than the respective Bohr exciton radius, the formation of bound states via the superposition of electron−hole pairs is negligible, which rationalizes our IOA approach. In Figure 3b, it is found that the optical absorption near the band edge is optically forbidden. Such an optically inactive character can be attributed to the indirect gap nature of Si. The intense absorption peaks stem from transitions with large oscillator strengths. There are four peaks (*i*−*iv*) in the spectrum, each of which is composed of certain groups of state-to-state transitions. The main components for the most intense peak at ∼2.6 eV (peak *ii*) correspond to the c → c′ and b → d′ features in the DOS. The leading contributions for other peaks are summarized in Table S2. Note, the absorption spectrum is derived from gamma-point calculations. In Figure S2, we compare DOS and absorption spectra from calculations using gamma-point only with 4 × 4 × 1 gamma-centered grids. This shows that orbitals from gamma-point only calculations indeed have characteristic momentum dependence, since the simulation cell is composed of multiple unit cells. Those orbital pairs originating from the same momentum give pronounced optical transitions.[47] However, except difference in peak intensities, the spectral features appear at the same energies for gamma- and momentum-dispersion distribution.

The electronic structures of the hydrogenated slab are shown in Figure S3. The HOMO−LUMO gap of the hydrogenated silicon slab is about 0.01 eV greater than that of the phenyl-covered slab. The absorption spectra for the passivated silicon slabs are quite similar despite some variations in the relative peak intensities. It is interesting that transitions between orbitals that keep the same number of nodal planes of the envelope function contribute higher intensity to the absorption (see Figure S4). The Kohn−Sham orbital can be represented as a product of two factors: the atomic part and the envelope function.[72] As such, a matrix element of the transition dipole for a pair of orbitals includes two terms: (i) the transition dipole matrix element between noncoinciding atomic functions multiplied by the Dirac delta function (for coinciding envelope functions) and (ii) the transition dipole between noncoinciding envelope functions multiplied by the overlap of atomic functions. Typically, the first term dominates resulting in an approximate “conservation” of envelope function during optical transitions.

Modeling of charge carrier dynamics relies on ambient-temperature AIMD trajectories, which enable the calculation of nonadiabatic couplings and elements of the Redfield tensor. Figure 3c shows a superposition of multiple atomic coordinates along the adiabatic molecular dynamics trajectory at 300 K. As expected, the displacement of surface Si atoms is more significant than that of interior Si atoms. We further compute the charge carrier dynamics upon photoexcitation. Here we

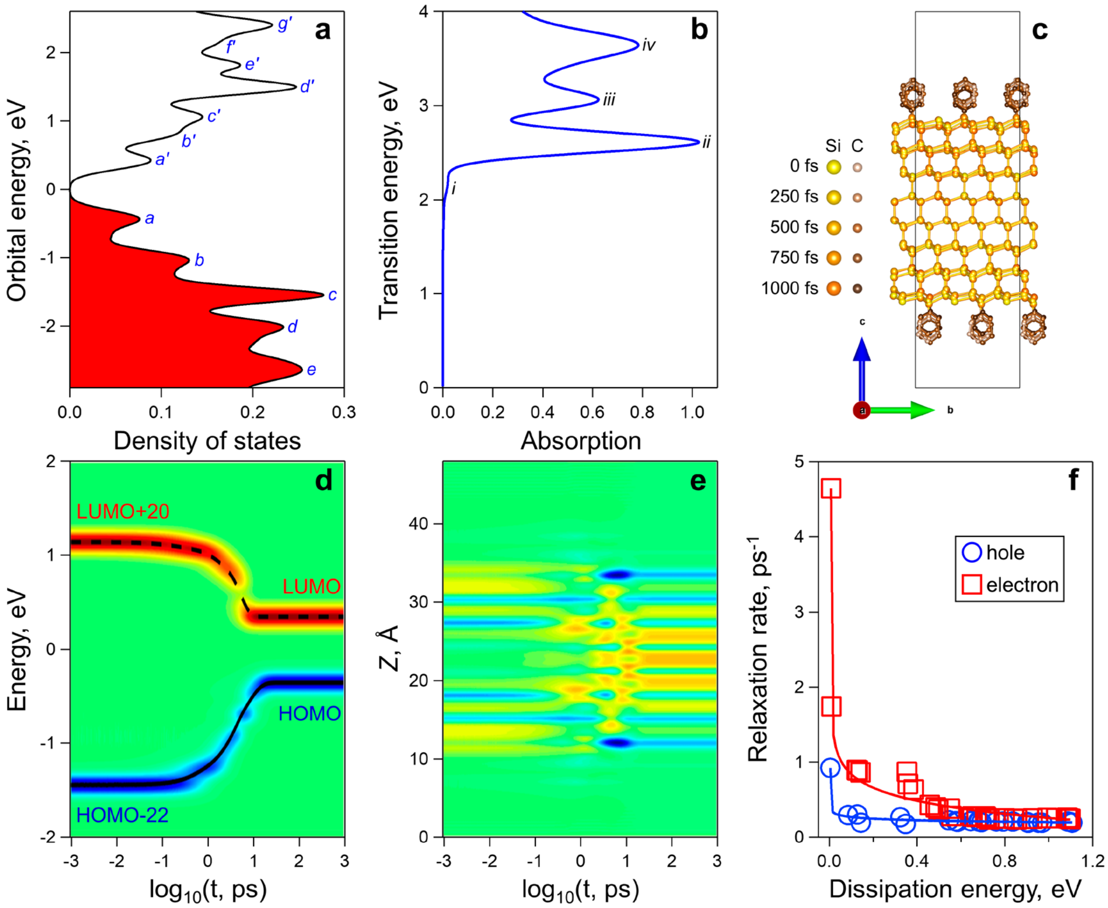

Figure 3. Calculated electronic structure and charge carrier dynamics for the $Si_{128}H_8Ph_8$ slab. (a) Density of states. The filled and empty areas correspond to occupied and empty orbitals, respectively. (b) Absorption spectrum. (c) Superposition of structures along the molecular dynamics trajectory at 300 K. Hydrogen atoms are not shown explicitly for clarity. (d) Evolution of charge carriers as a function of energy and time. Black (solid and dashed) lines denote expectation values. (e) Dynamics of spatial distribution of charge carriers. The charge distribution shows that during 1−100 fs both electron and hole have similar envelope functions with two nodal planes. At later times, most pronounced in the interval during 2−10 ps, spatial localizations of electron and hole differ by being localized in the center of the slab and near the surface, respectively. In panels d and e, color codes red, green, and blue represent the distribution for gain, no change, and loss of the charge, respectively, relative to the equilibrium distribution. The initial excitation is from HOMO−22 to LUMO+20, corresponding to the *ii* absorption peak (c → c′). In panels a and d, the energy is shifted with reference to the Fermi level, which is defined as the midpoint of the HOMO−LUMO gap. (f) Nonradiative relaxation rates of charge carriers under different initial conditions.

assume that there is an instantaneous photoexcitation at $t < 0$, forming a hot hole in a VB orbital and a hot electron in a CB orbital. Figure 3d depicts a representative example of charge carrier relaxation as a function of energy and time following an initial photoexcitation from HOMO−22 to LUMO+20 for the $Si_{128}H_8Ph_8$ slab. Here, the initial photoexcitation corresponds to the absorption peak *ii* with contributions from c → c′ features in the DOS being one of the most optically active transitions for the slab. In Figure 3d, the red and blue isocontours represent gain and loss of the electron density with respect to the equilibrium distribution, respectively. Initially, an electron and a hole reside at LUMO+20 and HOMO−22 orbitals, respectively. The hot charge carriers then gradually approach band edges with time through the dissipation of electronic energy into lattice vibrations. The relaxation rate of an electron is greater than that of a hole. Finally, LUMO and HOMO are getting occupied by charge carriers, followed by the recombination of electron and hole occurring on a much longer ~0.2 ns^{-1} time scale.

In Figure 3e, we track the evolution of charge carriers in real space by projecting their charge density distribution onto the normal direction. Note, Figure 3e is scaled according to Figure 3c. We find that after the completion of relaxation, the charge carriers reside at frontier orbitals with charge density distribution mainly located on the interior Si atoms. Another interesting observation is that there is a nonzero contribution from the surface phenyl groups during the relaxation of hot carriers. We also calculate relaxation rates of charge carriers under different initial conditions for the $Si_{128}H_8Ph_8$ slab. The procedure to extract rates from the dynamics has been discussed in the work by Talgat et al.[55] In Figure 3f, the relaxation rate is plotted as a function of dissipated energy. Here the dissipated energy is defined as the relative energy of the initial excited orbital with respect to the frontier orbital. Figure 3f shows that relaxation rates of electrons are higher than that of holes. At higher dissipation energies, the difference between the relaxation rates of electrons and holes is minimal. With decreasing dissipation energies, the difference becomes more significant.

Charge carrier dynamics for the hydrogenated silicon slab are shown in Figure S3. The evaluated recombination rate of the electron and hole is ~89.2 ns^{-1}, which is significantly

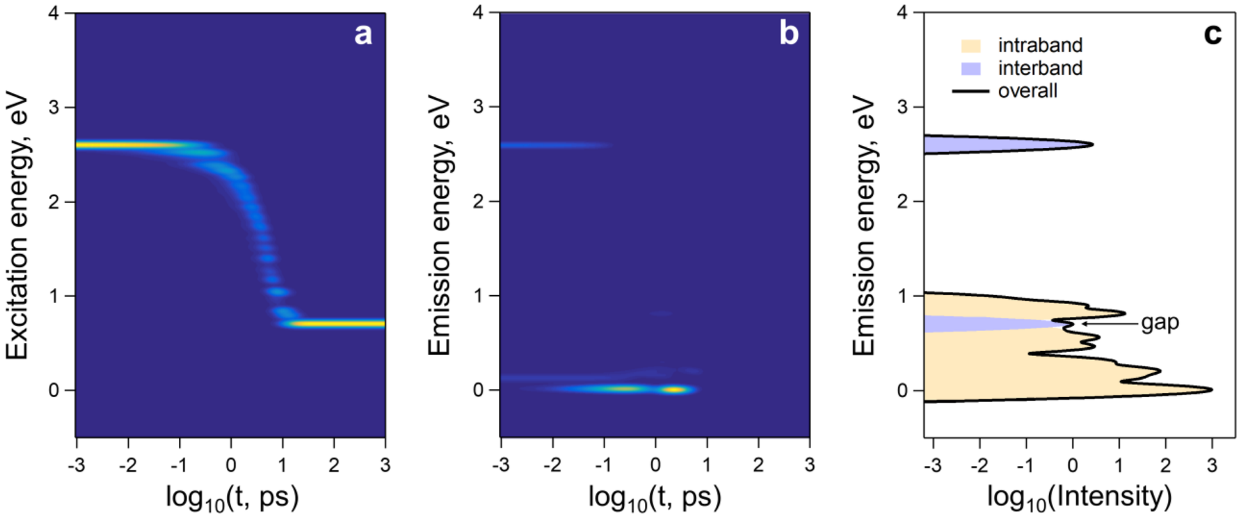

Figure 4. Computed relaxation dynamics of the $Si_{128}H_8Ph_8$ slab following the initial excitation from HOMO−22 to LUMO+20, corresponding to the *ii* absorption peak (c → c′). (a) Dynamics of excitation energy dissipation. (b) Time resolved emission spectrum. (c) Time integrated emission spectrum. In panels a and b, population of energy is shown at the maximum in yellow and minimum in blue.

greater than the value derived for the phenyl-terminated slab (~0.2 ns^{-1}). It is also important to note that the hydrogenated slab shows greater relaxation rates of hot charge carriers than that of the phenyl-terminated slab. A possible explanation is that heavier surface ligands constrain the motion of Si surface atoms, thus suppressing cooling and recombination.[73] In fact, several factors could contribute to suppressing nonadiabatic relaxation channels, including the symmetry of orbitals, phonon frequencies coupled to excited states, subgaps above the band edge, and trap states.[74] For both hydrogenated and phenyl-covered models, we find that relaxation rates of charge carriers decrease with increasing dissipation energies, in accordance with the gap law.[75]

Figure 4a shows the dissipation of excitation energy into lattice vibrations as a function of time for the $Si_{128}H_8Ph_8$ slab. Initially, we observe a strong feature at ~2.6 eV corresponding to the initial photoexcitation from HOMO−22 to LUMO+20. The nonradiative relaxation events mainly take place during ~0.1−10 ps, where several short-lived features with low population are observed. After ~10 ps, charge carriers arrive to frontier orbitals, and thus a long-living transition at ~0.7 eV corresponding to the HOMO−LUMO gap is clearly observed. A concomitant radiative relaxation is in competition with nonradiative relaxation following photoexcitation. Figure 4b shows the time-resolved emission spectrum calculated under the same initial condition as in Figure 4a. Immediately after the initial photoexcitation, we observe two optically strong features at ~2.6 and ~0.2 eV, respectively. The former corresponds to the parent interband emission from LUMO+22 to HOMO−20, which disappears at ~0.1 ps due to dominating nonradiative loss. The later feature at ~0.2 eV comes from the intraband transitions within the CB or VB. Starting from ~3 fs, we detect additional long-living low-energy intraband feature. Both intraband peaks vanish ~10 ps after the charge carriers reach the band edges. Note that the long-lived interband LUMO → HOMO transition (~0.7 eV) is optically weak and hardly resolved in Figure 4b.

Figure 4c shows the time-integrated emission from Figure 4b. Two interband peaks (LUMO+22 → HOMO−20 and LUMO → HOMO) can be assigned to Γ−Γ transitions with conservation of momentum and Γ−X without conservation of momentum, respectively. The other low-energy peaks arise from intraband emissions. The absence of long-lived intermediate states during the relaxation process limits the number of interband peaks. In addition, the intraband emissions are dominant over interband ones, as there are more relaxation channels and greater transition probabilities for the former. Similar trends in time-resolved and time-integrated emission spectra are observed for the hydrogenated silicon model (Figure S5). While radiative rates are comparable between phenyl- and hydrogen-terminated slabs, much slower nonradiative transitions in $Si_{128}H_8Ph_8$ result in higher quantum yield of emission, compared to $Si_{128}H_{16}$; see Table S3.

In summary, we performed AIMD calculations to model the thermal grafting of benzenediazonium bromide onto hydrogenated Si(111) surfaces. A sequence of reaction steps is identified in the AIMD trajectory, including the loss of N_2 from the diazonium salt, proton transfer from the surface to the bromide ion that eliminates HBr, and attachment of the phenyl group onto the surface. The identified reaction steps agree well with experimental data.[70,71] Such an addition of phenyl groups substantially modifies optoelectronic properties of hydrogenated Si(111) slabs. By conducting nonadiabatic-coupling calculations using a combination of *ab initio* results and reduced density matrix formalism with Redfield theory, we further detail the charge carrier dynamics of passivated Si(111) slabs upon photoexcitation. The phenyl-terminated slab shows reduced nonradiative relaxation and recombination rates of hot charge carriers compared to the hydrogen-terminated slab, because heavier surface ligands restrict the motion of Si surface atoms in the nonadiabatic relaxation channel. This work illustrates that, first, the diazonium salt thermally decomposes in the vicinity of the silicon surface allowing the formation of a covalently bonded phenyl group, and, second, the coverage of phenyl groups on the silicon surface slows down charge-carrier cooling driven by electron−phonon interactions, which noticeably increases the emission quantum yield compared to hydrogenated silicon slab. Our findings thus contribute to the continuous development of synthetic routes targeting functionalization of semiconductor surfaces with diazonium salts. The treated semiconductors with improved stabilities and prolonged charge carrier lifetimes are expected to have improved performance in photovoltaic and optoelectronic applications.

■ ASSOCIATED CONTENT

Supporting Information

The Supporting Information is available free of charge at https://pubs.acs.org/doi/10.1021/acs.jpclett.1c02084.

Computational details, Bader charge analysis, ground state observables, charge carrier dynamics, and photoluminescence (PDF)

Video S1 (MP4)

Video S2 (MP4)

■ AUTHOR INFORMATION

Corresponding Author

Dmitri S. Kilin − *Department of Chemistry and Biochemistry, North Dakota State University, Fargo, North Dakota 58108, United States;* orcid.org/0000-0001-7847-5549; Email: dmitri.kilin@ndsu.edu

Authors

Yulun Han − *Department of Chemistry and Biochemistry, North Dakota State University, Fargo, North Dakota 58108, United States;* orcid.org/0000-0002-8619-0233

Kweeni Iduoku − *Department of Coatings and Polymeric Materials, North Dakota State University, Fargo, North Dakota 58108, United States*

Gena Grant − *Turtle Mountain Community College, Belcourt, North Dakota 58316, United States*

Bakhtiyor Rasulev − *Department of Coatings and Polymeric Materials, North Dakota State University, Fargo, North Dakota 58108, United States;* orcid.org/0000-0002-7845-4884

Alexey Leontyev − *Department of Chemistry and Biochemistry, North Dakota State University, Fargo, North Dakota 58108, United States;* orcid.org/0000-0003-0219-709X

Erik K. Hobbie − *Department of Physics, North Dakota State University, Fargo, North Dakota 58108, United States*

Sergei Tretiak − *Theoretical Division and Center for Integrated Nanotechnologies, Los Alamos National Laboratory, Los Alamos, New Mexico 87545, United States;* orcid.org/0000-0001-5547-3647

Svetlana V. Kilina − *Department of Chemistry and Biochemistry, North Dakota State University, Fargo, North Dakota 58108, United States;* orcid.org/0000-0003-1350-2790

Complete contact information is available at: https://pubs.acs.org/10.1021/acs.jpclett.1c02084

Notes

The authors declare no competing financial interest.

■ ACKNOWLEDGMENTS

Authors thank DOE BES NERSC facility for computational resources, Allocation Award #91202, “Computational Modeling of Photo-catalysis and Photo-induced Charge Transfer Dynamics on Surfaces” supported by the Office of Science of the DOE under Contract No. DE-AC02-05CH11231. This work used resources of the Center for Computationally Assisted Science and Technology (CCAST) at North Dakota State University, which were made possible in part by NSF MRI Award No. 2019077. This work is also supported in part by the National Science Foundation through Grant No. CHE-1944921. S.V.K. acknowledges partial financial support from NSF CHE-2004197. D.S.K. and K.I. gratefully acknowledge support of the program “ND EPSCoR: Advancing Science Excellence in ND: Subaward: CI: Preliminary Data: Photochemistry and Photophysics of Silicon Surfaces”. This work was conducted in part at the Center for Integrated Nanotechnologies, a U.S. Department of Energy, Office of Science, user facility and supported in part by Los Alamos National Laboratory Directed Research and Development funds.

■ REFERENCES

(1) Trucks, G. W.; Raghavachari, K.; Higashi, G. S.; Chabal, Y. J. Mechanism of HF etching of silicon surfaces: A theoretical understanding of hydrogen passivation. *Phys. Rev. Lett.* **1990**, *65* (4), 504−507.

(2) Kern, W. The Evolution of Silicon Wafer Cleaning Technology. *J. Electrochem. Soc.* **1990**, *137* (6), 1887−1892.

(3) Niwano, M.; Kimura, Y.; Miyamoto, N. In situ Infrared Study of Chemical State of Si Surface in Etching Solution. *Appl. Phys. Lett.* **1994**, *65* (13), 1692−1694.

(4) Wong, K. T.; Lewis, N. S. What a Difference a Bond Makes: The Structural, Chemical, and Physical Properties of Methyl-Terminated Si(111) Surfaces. *Acc. Chem. Res.* **2014**, *47* (10), 3037−3044.

(5) Scheres, L.; Giesbers, M.; Zuilhof, H. Organic Monolayers onto Oxide-Free Silicon with Improved Surface Coverage: Alkynes versus Alkenes. *Langmuir* **2010**, *26* (7), 4790−4795.

(6) Reboredo, F. A.; Galli, G. Theory of Alkyl-Terminated Silicon Quantum Dots. *J. Phys. Chem. B* **2005**, *109* (3), 1072−1078.

(7) Pujari, S. P.; Filippov, A. D.; Gangarapu, S.; Zuilhof, H. High-Density Modification of H-Terminated Si(111) Surfaces Using Short-Chain Alkynes. *Langmuir* **2017**, *33* (51), 14599−14607.

(8) Yu, H.; Webb, L. J.; Ries, R. S.; Solares, S. D.; Goddard, W. A.; Heath, J. R.; Lewis, N. S. Low-Temperature STM Images of Methyl-Terminated Si(111) Surfaces. *J. Phys. Chem. B* **2005**, *109* (2), 671−674.

(9) Nemanick, E. J.; Hurley, P. T.; Brunschwig, B. S.; Lewis, N. S. Chemical and Electrical Passivation of Silicon (111) Surfaces through Functionalization with Sterically Hindered Alkyl Groups. *J. Phys. Chem. B* **2006**, *110* (30), 14800−14808.

(10) Liu, X.; Zhao, S.; Gu, W.; Zhang, Y.; Qiao, X.; Ni, Z.; Pi, X.; Yang, D. Light-Emitting Diodes Based on Colloidal Silicon Quantum Dots with Octyl and Phenylpropyl Ligands. *ACS Appl. Mater. Interfaces* **2018**, *10* (6), 5959−5966.

(11) Soria, F. A.; Zhang, W.; Paredes-Olivera, P. A.; van Duin, A. C. T.; Patrito, E. M. Si/C/H ReaxFF Reactive Potential for Silicon Surfaces Grafted with Organic Molecules. *J. Phys. Chem. C* **2018**, *122* (41), 23515−23527.

(12) Terry, J.; Linford, M. R.; Wigren, C.; Cao, R.; Pianetta, P.; Chidsey, C. E. D. Alkyl-terminated Si(111) surfaces: A High-resolution, Core Level Photoelectron Spectroscopy Study. *J. Appl. Phys.* **1999**, *85* (1), 213−221.

(13) Webb, L. J.; Nemanick, E. J.; Biteen, J. S.; Knapp, D. W.; Michalak, D. J.; Traub, M. C.; Chan, A. S. Y.; Brunschwig, B. S.; Lewis, N. S. High-Resolution X-ray Photoelectron Spectroscopic Studies of Alkylated Silicon(111) Surfaces. *J. Phys. Chem. B* **2005**, *109* (9), 3930−3937.

(14) Linford, M. R.; Fenter, P.; Eisenberger, P. M.; Chidsey, C. E. D. Alkyl Monolayers on Silicon Prepared from 1-Alkenes and Hydrogen-Terminated Silicon. *J. Am. Chem. Soc.* **1995**, *117* (11), 3145−3155.

(15) Sieval, A. B.; Demirel, A. L.; Nissink, J. W. M.; Linford, M. R.; van der Maas, J. H.; de Jeu, W. H.; Zuilhof, H.; Sudhölter, E. J. R. Highly Stable Si−C Linked Functionalized Monolayers on the Silicon (100). *Langmuir* **1998**, *14* (7), 1759−1768.

(16) Cottineau, T.; Morin, M.; Bélanger, D. Surface Band Structure of Aryl-diazonium Modified p-Si electrodes Determined by X-ray

Photoelectron Spectroscopy and Electrochemical Measurements. *RSC Adv.* **2013**, *3* (45), 23649−23657.

(17) Nemanick, E. J.; Solares, S. D.; Goddard, W. A.; Lewis, N. S. Quantum Mechanics Calculations of the Thermodynamically Controlled Coverage and Structure of Alkyl Monolayers on Si(111) Surfaces. *J. Phys. Chem. B* **2006**, *110*, 14842−14848.

(18) Bélanger, D.; Pinson, J. Electrografting: A Powerful Method for Surface Modification. *Chem. Soc. Rev.* **2011**, *40* (7), 3995−4048.

(19) Mahouche-Chergui, S.; Gam-Derouich, S.; Mangeney, C.; Chehimi, M. M. Aryl Diazonium Salts: A New Class of Coupling Agents for Bonding Polymers, Biomacromolecules and Nanoparticles to Surfaces. *Chem. Soc. Rev.* **2011**, *40* (7), 4143−4166.

(20) Stewart, M. P.; Maya, F.; Kosynkin, D. V.; Dirk, S. M.; Stapleton, J. J.; McGuiness, C. L.; Allara, D. L.; Tour, J. M. Direct Covalent Grafting of Conjugated Molecules onto Si, GaAs, and Pd Surfaces from Aryldiazonium Salts. *J. Am. Chem. Soc.* **2004**, *126* (1), 370−378.

(21) Gifford, B. J.; Kilina, S.; Htoon, H.; Doorn, S. K.; Tretiak, S. Controlling Defect-State Photophysics in Covalently Functionalized Single-Walled Carbon Nanotubes. *Acc. Chem. Res.* **2020**, *53* (9), 1791−1801.

(22) He, X.; Gifford, B. J.; Hartmann, N. F.; Ihly, R.; Ma, X.; Kilina, S. V.; Luo, Y.; Shayan, K.; Strauf, S.; Blackburn, J. L.; et al. Low-Temperature Single Carbon Nanotube Spectroscopy of sp3 Quantum Defects. *ACS Nano* **2017**, *11* (11), 10785−10796.

(23) Bouriga, M.; Chehimi, M. M.; Combellas, C.; Decorse, P.; Kanoufi, F.; Deronzier, A.; Pinson, J. Sensitized Photografting of Diazonium Salts by Visible Light. *Chem. Mater.* **2013**, *25* (1), 90−97.

(24) Chen, B.; Flatt, A. K.; Jian, H.; Hudson, J. L.; Tour, J. M. Molecular Grafting to Silicon Surfaces in Air Using Organic Triazenes as Stable Diazonium Sources and HF as a Constant Hydride-Passivation Source. *Chem. Mater.* **2005**, *17* (19), 4832−4836.

(25) Höhlein, I. M. D.; Kehrle, J.; Helbich, T.; Yang, Z.; Veinot, J. G. C.; Rieger, B. Diazonium Salts as Grafting Agents and Efficient Radical-Hydrosilylation Initiators for Freestanding Photoluminescent Silicon Nanocrystals. *Chem. - Eur. J.* **2014**, *20* (15), 4212−4216.

(26) Shi, L.; Sun, T.; Yan, Y.; Zhao, J.; Dong, S. Fabrication of Functional Structures at Si (100) Surface by Mechanical Scribing in the Presence of Aryl Diazonium Salts. *J. Vac. Sci. Technol., B* **2009**, *27* (3), 1399−1402.

(27) Mirkhalaf, F.; Mason, T. J.; Morgan, D. J.; Saez, V. Frequency Effects on the Surface Coverage of Nitrophenyl Films Ultrasonically Grafted onto Indium Tin Oxide. *Langmuir* **2011**, *27* (5), 1853−1858.

(28) Kilina, S.; Kilin, D.; Tretiak, S. Light-Driven and Phonon-Assisted Dynamics in Organic and Semiconductor Nanostructures. *Chem. Rev.* **2015**, *115* (12), 5929−5978.

(29) Kilina, S. V.; Tamukong, P. K.; Kilin, D. S. Surface Chemistry of Semiconducting Quantum Dots: Theoretical Perspectives. *Acc. Chem. Res.* **2016**, *49* (10), 2127−2135.

(30) Li, X.; Tully, J. C.; Schlegel, H. B.; Frisch, M. J. Ab initio Ehrenfest dynamics. *J. Chem. Phys.* **2005**, *123* (8), 084106.

(31) Tully, J. C.; Preston, R. K. Trajectory Surface Hopping Approach to Nonadiabatic Molecular Collisions: The Reaction of H+ with D2. *J. Chem. Phys.* **1971**, *55* (2), 562−572.

(32) Tully, J. C. Molecular Dynamics with Electronic Transitions. *J. Chem. Phys.* **1990**, *93* (2), 1061−1071.

(33) Redfield, A. G. On the Theory of Relaxation Processes. *IBM J. Res. Dev.* **1957**, *1* (1), 19−31.

(34) Jean, J. M.; Friesner, R. A.; Fleming, G. R. Application of A Multilevel Redfield Theory to Electron Transfer in Condensed Phases. *J. Chem. Phys.* **1992**, *96* (8), 5827−5842.

(35) Vincent, J. C.; Muuronen, M.; Pearce, K. C.; Mohanam, L. N.; Tapavicza, E.; Furche, F. That Little Extra Kick: Nonadiabatic Effects in Acetaldehyde Photodissociation. *J. Phys. Chem. Lett.* **2016**, *7* (20), 4185−4190.

(36) Ondarse-Alvarez, D.; Nelson, T.; Lupton, J. M.; Tretiak, S.; Fernandez-Alberti, S. Let Digons be Bygones: The Fate of Excitons in Curved *π*-Systems. *J. Phys. Chem. Lett.* **2018**, *9* (24), 7123−7129.

(37) Tao, H.; Levine, B. G.; Martínez, T. J. Ab Initio Multiple Spawning Dynamics Using Multi-State Second-Order Perturbation Theory. *J. Phys. Chem. A* **2009**, *113* (49), 13656−13662.

(38) Nelson, T. R.; Ondarse-Alvarez, D.; Oldani, N.; Rodriguez-Hernandez, B.; Alfonso-Hernandez, L.; Galindo, J. F.; Kleiman, V. D.; Fernandez-Alberti, S.; Roitberg, A. E.; Tretiak, S. Coherent Exciton-vibrational Dynamics and Energy Transfer in Conjugated Organics. *Nat. Commun.* **2018**, *9* (1), 2316.

(39) Nelson, T.; Fernandez-Alberti, S.; Roitberg, A. E.; Tretiak, S. Electronic Delocalization, Vibrational Dynamics, and Energy Transfer in Organic Chromophores. *J. Phys. Chem. Lett.* **2017**, *8* (13), 3020−3031.

(40) Alfonso Hernandez, L.; Nelson, T.; Gelin, M. F.; Lupton, J. M.; Tretiak, S.; Fernandez-Alberti, S. Interference of Interchromophoric Energy-Transfer Pathways in *π*-Conjugated Macrocycles. *J. Phys. Chem. Lett.* **2016**, *7* (23), 4936−4944.

(41) Han, Y.; Anderson, K.; Hobbie, E. K.; Boudjouk, P.; Kilin, D. S. Unraveling Photodimerization of Cyclohexasilane from Molecular Dynamics Studies. *J. Phys. Chem. Lett.* **2018**, *9* (15), 4349−4354.

(42) Kilin, D. S.; Micha, D. A. Modeling the Photovoltage of Doped Si Surfaces. *J. Phys. Chem. C* **2011**, *115* (3), 770−775.

(43) Vazhappilly, T.; Kilin, D. S.; Micha, D. A. Photoabsorbance and Photovoltage of Crystalline and Amorphous Silicon Slabs with Silver Adsorbates. *J. Phys. Chem. C* **2012**, *116* (48), 25525−25536.

(44) Kryjevski, A.; Mihaylov, D.; Kilin, D. Dynamics of Charge Transfer and Multiple Exciton Generation in the Doped Silicon Quantum Dot−Carbon Nanotube System: Density Functional Theory-Based Computation. *J. Phys. Chem. Lett.* **2018**, *9* (19), 5759−5764.

(45) Chen, J.; Schmitz, A.; Inerbaev, T.; Meng, Q.; Kilina, S.; Tretiak, S.; Kilin, D. S. First-Principles Study of p-n-Doped Silicon Quantum Dots: Charge Transfer, Energy Dissipation, and Time-Resolved Emission. *J. Phys. Chem. Lett.* **2013**, *4* (17), 2906−2913.

(46) Pringle, T. A.; Hunter, K. I.; Brumberg, A.; Anderson, K. J.; Fagan, J. A.; Thomas, S. A.; Petersen, R. J.; Sefannaser, M.; Han, Y.; Brown, S. L.; et al. Bright Silicon Nanocrystals from a Liquid Precursor: Quasi-Direct Recombination with High Quantum Yield. *ACS Nano* **2020**, *14* (4), 3858−3867.

(47) Fatima; Han, Y.; Vogel, D. J.; Inerbaev, T. M.; Oncel, N.; Hobbie, E. K.; Kilin, D. S. . Photoexcited Electron Lifetimes Influenced by Momentum Dispersion in Silicon Nanowires. *J. Phys. Chem. C* **2019**, *123* (12), 7457−7466.

(48) Han, Y.; Micha, D. A.; Kilin, D. S. Ab initio Study of the Photocurrent at the Au/Si Metal−semiconductor Nanointerface. *Mol. Phys.* **2015**, *113* (3−4), 327−335.

(49) Han, Y.; Tretiak, S.; Kilin, D. Dynamics of Charge Transfer at Au/Si Metal-semiconductor Nano-interface. *Mol. Phys.* **2014**, *112* (3−4), 474−484.

(50) Peng, W.-T.; Fales, B. S.; Shu, Y.; Levine, B. G. Dynamics of Recombination via Conical Intersection in a Semiconductor Nanocrystal. *Chem. Sci.* **2018**, *9* (3), 681−687.

(51) Shu, Y.; Fales, B. S.; Levine, B. G. Defect-Induced Conical Intersections Promote Nonradiative Recombination. *Nano Lett.* **2015**, *15* (9), 6247−6253.

(52) Meng, Q.; May, P. S.; Berry, M. T.; Kilin, D. Sequential Hydrogen Dissociation from A Charged Pt13H24 Cluster Modeled by ab initio Molecular Dynamics. *Int. J. Quantum Chem.* **2012**, *112* (24), 3896−3903.

(53) Han, Y.; Hobbie, E. K.; Kilin, D. S. First-Principles Molecular Dynamics of Monomethylhydrazine and Nitrogen Dioxide. *J. Phys. Chem. Lett.* **2019**, *10* (10), 2394−2399.

(54) Meng, Q.; Chen, J.; Kilin, D. Proton Reduction at Surface of Transition Metal Nanocatalysts. *Mol. Simul.* **2015**, *41* (1−3), 134−145.

(55) Inerbaev, T. M.; Hoefelmeyer, J. D.; Kilin, D. S. Photoinduced Charge Transfer from Titania to Surface Doping Site. *J. Phys. Chem. C* **2013**, *117* (19), 9673−9692.

(56) Forde, A.; Inerbaev, T.; Hobbie, E. K.; Kilin, D. S. Excited-State Dynamics of a CsPbBr3 Nanocrystal Terminated with Binary

Ligands: Sparse Density of States with Giant Spin−Orbit Coupling Suppresses Carrier Cooling. *J. Am. Chem. Soc.* **2019**, *141* (10), 4388−4397.

(57) Han, Y.; Meng, Q.; Rasulev, B.; May, P. S.; Berry, M. T.; Kilin, D. S. Photoinduced Charge Transfer versus Fragmentation Pathways in Lanthanum Cyclopentadienyl Complexes. *J. Chem. Theory Comput.* **2017**, *13* (9), 4281−4296.

(58) Kohn, W.; Sham, L. J. Self-Consistent Equations Including Exchange and Correlation Effects. *Phys. Rev.* **1965**, *140* (4A), A1133−A1138.

(59) Kresse, G.; Hafner, J. Ab initio Molecular Dynamics for Liquid Metals. *Phys. Rev. B: Condens. Matter Mater. Phys.* **1993**, *47* (1), 558−561.

(60) Kresse, G.; Hafner, J. Ab initio Molecular-Dynamics Simulation of the Liquid-Metal−Amorphous-Semiconductor Transition in Germanium. *Phys. Rev. B: Condens. Matter Mater. Phys.* **1994**, *49* (20), 14251−14269.

(61) Kresse, G.; Furthmüller, J. Efficient iterative schemes for ab initio total-energy calculations using a plane-wave basis set. *Phys. Rev. B: Condens. Matter Mater. Phys.* **1996**, *54* (16), 11169−11186.

(62) Kresse, G.; Furthmüller, J. Efficiency of ab-initio Total Energy Calculations for Metals and Semiconductors Using a Plane-Wave Basis Set. *Comput. Mater. Sci.* **1996**, *6* (1), 15−50.

(63) Blöchl, P. E. Projector Augmented-wave Method. *Phys. Rev. B: Condens. Matter Mater. Phys.* **1994**, *50* (24), 17953−17979.

(64) Perdew, J. P.; Chevary, J. A.; Vosko, S. H.; Jackson, K. A.; Pederson, M. R.; Singh, D. J.; Fiolhais, C. Atoms, molecules, solids, and surfaces: Applications of the generalized gradient approximation for exchange and correlation. *Phys. Rev. B: Condens. Matter Mater. Phys.* **1992**, *46* (11), 6671−6687.

(65) Perdew, J. P.; Burke, K.; Ernzerhof, M. Generalized Gradient Approximation Made Simple. *Phys. Rev. Lett.* **1996**, *77* (18), 3865−3868.

(66) Grimme, S. Semiempirical GGA-type Density Functional Constructed with A Long-range Dispersion Correction. *J. Comput. Chem.* **2006**, *27* (15), 1787−1799.

(67) Tang, W.; Sanville, E.; Henkelman, G. A Grid-based Bader Analysis Algorithm without Lattice Bias. *J. Phys.: Condens. Matter* **2009**, *21* (8), 084204.

(68) Sanville, E.; Kenny, S. D.; Smith, R.; Henkelman, G. Improved Grid-based Algorithm for Bader Charge Allocation. *J. Comput. Chem.* **2007**, *28* (5), 899−908.

(69) Henkelman, G.; Arnaldsson, A.; Jónsson, H. A Fast and Robust Algorithm for Bader Decomposition of Charge Density. *Comput. Mater. Sci.* **2006**, *36* (3), 354−360.

(70) Pandey, D.; Zemlyanov, D. Y.; Bevan, K.; Reifenberger, R. G.; Dirk, S. M.; Howell, S. W.; Wheeler, D. R. UHV STM I(V) and XPS Studies of Aryl Diazonium Molecules Assembled on Si(111). *Langmuir* **2007**, *23* (9), 4700−4708.

(71) Allongue, P.; Henry de Villeneuve, C.; Cherouvrier, G.; Cortès, R.; Bernard, M. C. Phenyl Layers on H−Si(111) by Electrochemical Reduction of Diazonium Salts: Monolayer versus Multilayer Formation. *J. Electroanal. Chem.* **2003**, *550−551*, 161−174.

(72) Kilin, D. S.; Micha, D. A. Surface Photovoltage at Nanostructures on Si Surfaces: Ab Initio Results. *J. Phys. Chem. C* **2009**, *113* (9), 3530−3542.

(73) Kilina, S. V.; Neukirch, A. J.; Habenicht, B. F.; Kilin, D. S.; Prezhdo, O. V. Quantum Zeno Effect Rationalizes the Phonon Bottleneck in Semiconductor Quantum Dots. *Phys. Rev. Lett.* **2013**, *110* (18), 180404.

(74) Wei, Y.; Fang, W.-H.; Long, R. Covalent Functionalized Black Phosphorus Greatly Inhibits Nonradiative Charge Recombination: A Time Domain Ab Initio Study. *J. Phys. Chem. Lett.* **2020**, *11* (2), 478−484.

(75) Vogel, D. J.; Kryjevski, A.; Inerbaev, T.; Kilin, D. S. Photoinduced Single- and Multiple-Electron Dynamics Processes Enhanced by Quantum Confinement in Lead Halide Perovskite Quantum Dots. *J. Phys. Chem. Lett.* **2017**, *8* (13), 3032−3039.

https://doi.org/10.1021/acs.jpclett.1c02084
J. Phys. Chem. Lett. 2021, 12, 7504−7511